Supplementary Information for:

Light-Induced Bimerons in a Chiral Magnet

Kaixin Zhu[1,2], Filipp N.Rybakov[3], Zhan Wang[1,2], Wenli Gao[1,4], Shuaishuai Sun[1], Wentao Wang[1,2], Jun Li[1], Huanfang Tian[1], Olle Eriksson[3], Huaixin Yang[1,2], Ying Zhang[1,2,5], Nikolai S. Kiselev*[6], Zian Li*[7], and Jianqi Li*[1,2,5]1

[11] *Beijing National Laboratory for Condensed Matter Physics, Institute of Physics, Chinese Academy of Sciences, Beijing 100190, China.*

[2] *School of Physical Sciences, University of Chinese Academy of Sciences, Beijing 100049, China.*

[3] *Department of Physics and Astronomy, Uppsala University, Uppsala, Sweden.*

[4] *School of Physics, Northwest University, Xi'an 710069, China*

[5] *Songshan Lake Materials Laboratory, Dongguan, Guangdong, 523808, China*

[6] *Peter Grünberg Institute, Forschungszentrum Jülich, Jülich, Germany.*

[7] *School of Physical Science and Technology, Guangxi University, Nanning 530004, China*

e-mail: n.kiselev@fz-juelich.de; zianli@gxu.edu.cn; ljq@iphy.ac.cn

1. The topological invariants of merons. In this section, we provide a brief summary of the main results from Ref.[1] that are relevant to the systems discussed in the present study. Let us consider a two-dimensional magnetic system defined in the xy-plane. In the presence of easy-plane anisotropy with the axis aligned along $\mathbf{e}_z$, magnetization pointing perpendicular to the plane, $\mathbf{m}(\mathbf{r}) = \pm\mathbf{e}_z$, is energetically unfavorable. The system tends to minimize the area where spins point perpendicular to the plane. In such cases, it is always possible to define a domain Ω such that, inside this domain, spins can take a value on the entire sphere ($\mathbf{m} \in \mathbb{S}^2$), while on the boundary $\partial\Omega$, they are effectively restricted to a sphere with two punctures corresponding to the poles: $\mathbf{m} \in \mathbb{S}^2 \setminus \{P_1, P_2\}$. It is assumed that the domain Ω is homeomorphic (topologically equivalent) to a disk or a square-shaped region. In this case, the corresponding classifying homotopy group is $\pi_2(\mathbb{S}^2, \mathbb{S}^2 \setminus P_1, P_2) =$

$\pi_2(\mathbb{S}^2 \vee \mathbb{S}^2, P_0) = \mathbb{Z} \times \mathbb{Z}$. This implies that the topological charge of a spin texture is defined by a pair of integers. These integers can be computed via an auxiliary mapping called the dumbbell projection[1]. This projection maps spins from the $\mathbb{S}^2$ sphere onto a manifold topologically equivalent to a wedge of two spheres—i.e., two spheres joined at a single point—resembling the shape of a dumbbell. This mapping is schematically illustrated in Fig.S1**a**–**d**, where the spheres are shown in cross-section. The magnetic textures projected onto each of these spheres—referred to as the top and bottom spheres—yield two distinct spin configurations, which must be normalized after projection. For brevity, we refer to these spin textures as the top ($\mathbf{m}_\mathrm{t}$) and bottom ($\mathbf{m}_\mathrm{b}$) projections, respectively. The topological charge can be represented by a pair of integers $(q_\mathrm{t}, q_\mathrm{b})$, where $q_\mathrm{t} = Q(\mathbf{m}_\mathrm{t})$ and $q_\mathrm{b} = Q(\mathbf{m}_\mathrm{b})$ are computed using Eq. (1) of the main text. By construction, $\mathbf{m}$t and $\mathbf{m}_\mathrm{b}$, are continuous and embedded in a ferromagnetic background, as illustrated by the four representative meron configurations shown in Fig. S1**e**–**h**.

The explicit equations for the dumbbell map can be written as follows[1]:

$$\mathbf{m}_\mathrm{t} = \begin{pmatrix} 2\gamma_\mathrm{t} m_x \\ 2\gamma_\mathrm{t} m_y \\ -1 + 2{\gamma_\mathrm{t}}^2(1+m_z)(1-\mu_\mathrm{t}) \end{pmatrix}, \tag{1}$$

where

$$\gamma_\mathrm{t} = \begin{cases} \sqrt{\dfrac{m_z - \mu_\mathrm{t}}{(1+m_z)(1-\mu_\mathrm{t})^2}} & \text{if} \quad \mu_\mathrm{t} < m_z, \\ 0 \quad \text{otherwise,} \end{cases}$$

and

$$\mathbf{m}_\mathrm{b} = \begin{pmatrix} 2\gamma_\mathrm{b} m_x \\ 2\gamma_\mathrm{b} m_y \\ 1 - 2{\gamma_\mathrm{b}}^2(1-m_z)(1+\mu_\mathrm{b}) \end{pmatrix}, \tag{2}$$

where

$$\gamma_\mathrm{b} = \begin{cases} \sqrt{\dfrac{\mu_\mathrm{b} - m_z}{(1-m_z)(1+\mu_\mathrm{b})^2}} & \text{if} \quad m_z < \mu_\mathrm{b}, \\ 0 \quad \text{otherwise.} \end{cases}$$

The parameters μ_t and μ_b characterizing the sizes of the top and bottom spheres of the dumbbell are defined as functions, $\mu_\mathrm{t} = +f(\rho)$, $\mu_\mathrm{b} = -f(\rho)$, where ρ is the reduced distance,

$\rho = 2\sqrt{(r_x/L_x)^2 + (r_y/L_y)^2}$, L_x and L_y represent the dimensions of the domain, r_x and r_y are coordinates relative to the domain center. Thereby, in the center of the domain $\rho = 0$ and near the boundaries $\rho = 1$. The function $f(\rho)$ can be any continuous function satisfying: $f(0) = 0$ and $f(1) = 1$, for instance simple linear function:

$$f(\rho) = \begin{cases} \rho & \text{for } \rho < 1, \\ 1 & \text{for } \rho \geq 1 \end{cases} \tag{3}$$

Figure S1**a-d** explains the geometrical meaning of these parameters. The black vector illustrates an arbitrary spin on a 2-sphere. The red and blue vectors illustrate the projection of this spin onto the top and bottom spheres, respectively. By projection here we mean dropping a perpendicular to the z-axis (see horizontal dashed line) and finding the intersection of this perpendicular with the sphere or a line segment connecting two spheres – handle of a dumbbell. Note that this line segment always corresponds to one of the poles of a sphere. As shown in Figure S1**c**, the projection into such a joint interval is equivalent to a projection to the corresponding pole (see red vector).

When the spin cannot be directly projected into a sphere, the projected vector is complemented by points at the poles of the spheres. For instance, the vector in Figure S1**a-c** does not have a direct projection to the bottom sphere, and we complement this projection by a vector pointing to the north pole of the bottom sphere.

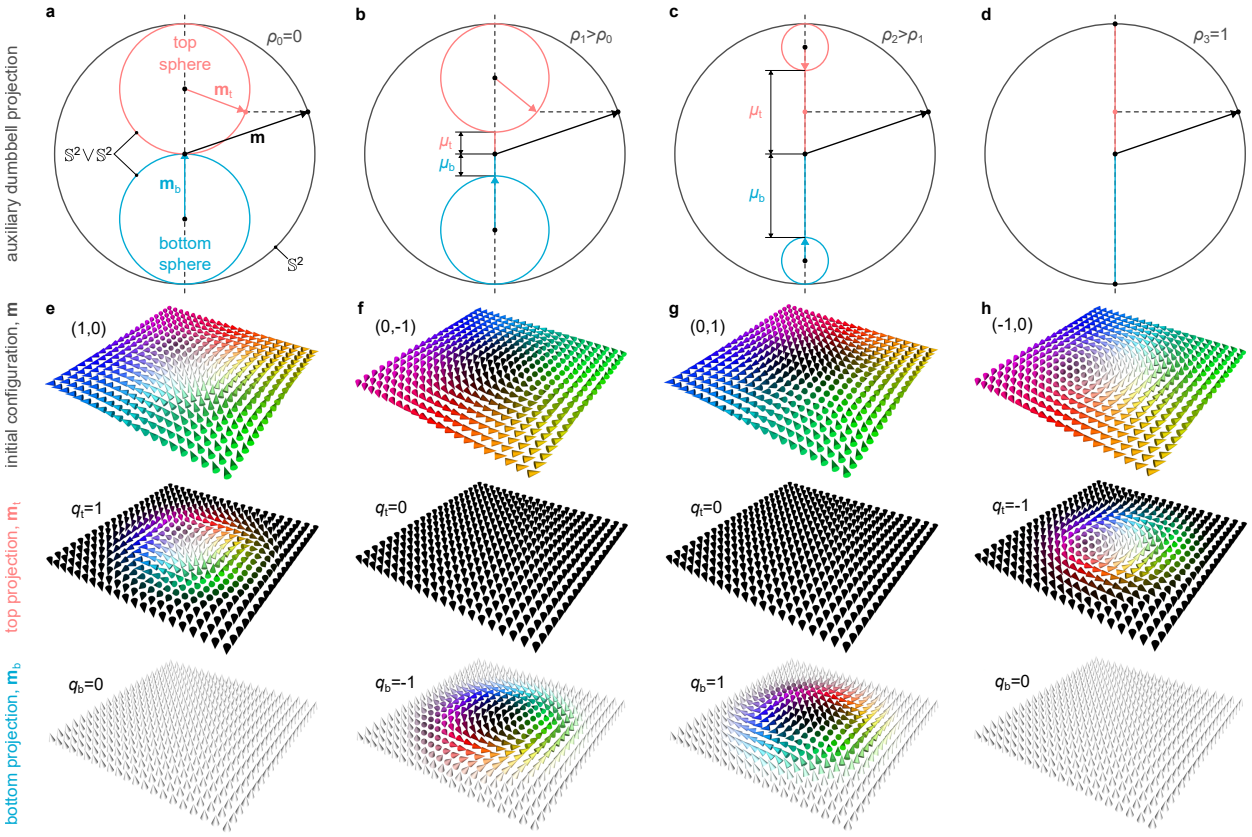

Figure S1. **Dumbbell projection and topological charge of individual merons.** The set of images **a**, **b**, **c**, and **d** illustrates the dumbbell projection described by Eqs. (1)-(3) for different values of parameter ρ – the normalized distance to the domain center. The four columns of images **e**–**h** schematically illustrate four merons with topological indices $(q_\mathrm{t}, q_\mathrm{b})$. The spin configurations labeled as top and bottom projections represent the result of applying the dumbbell projection to the corresponding vector field of the meron, resulting in two spin textures. The topological indices q_t and q_t correspond to Kronecker integral Q calculated for top and bottom protections, respectively. For details, see Ref.[1].

2. Sample characterization and ground-state. Bulk $Co_8Zn_8Mn_4$ exhibits a [111]-oriented hard magnetic axis. The temperature dependence of sample saturation magnetization is shown in Fig. S2. In this study, we fabricated thin $Co_8Zn_8Mn_4$ plate with orientations near the [111] zone axis. For thick films (with thickness above 200 nm), the properties resemble those of bulk material. In particular, the ground state in such thick samples is a helix with **k**-vector lying in the plane as depicted in Fig. S3**c**. The equilibrium period of helix is $L_{\mathrm{D}} = 140$ nm. When the plate thickness decreases below $1L_{\mathrm{D}}$, shape-induced in-plane anisotropy favors helix with **k**-vector pointing perpendicular to the plate. Such helix states should exhibit no contrasts in Lorentz TEM images due to zero integral in-plane magnetization component along the depth. However, due to the surface twist effect in the chiral magnet thin plate, an additional surface modulations are generated on the surfaces of the sample[2]. These surface modulations give rise to additional weak contrast in Lorentz TEM, especially at low magnetic field, see Fig. S3**b**. The intensity of surface modulations oscillates with variations in thickness. This effect becomes pronounced exclusively in very thin films[2,3]. From Fig. S3**a** and **b**, it is evident that as thickness decreases from 140 nm to 90 nm, the surface modulations intensity undergoes approximately half an oscillation cycle, yielding weaker contrast at the 140 nm sample and stronger contrast at the 90 nm sample. The domain in 90 nm sample dynamically evolves into bimeron structures under laser pulse excitation. Micromagnetic simulations were performed on three samples with corresponding thicknesses, reproducing the three ground-state domain configurations.

Figure S4 characterizes the two experimental samples used in the main text. Figures S4**a** and **c** show the Lorentz TEM images of thin and thick samples, respectively. Observation areas ($\sim 2.5\,\mu$m $\times$ 2.5μm) are marked by red boxes: the region in Fig. S4**a** has an average thickness of $\sim 0.65L_{\mathrm{D}}$, and that in Fig. S4**c** measures $\sim 1L_{\mathrm{D}}$. Figures S4**b** and **d** display the mean thickness profiles along the direction marked by the dashed arrows. These profiles were obtained through 1 μm step scanning via electron energy loss spectroscopy (EELS), with thickness values calculated from the absolute ratio of acquired spectra to the zero-loss peak.

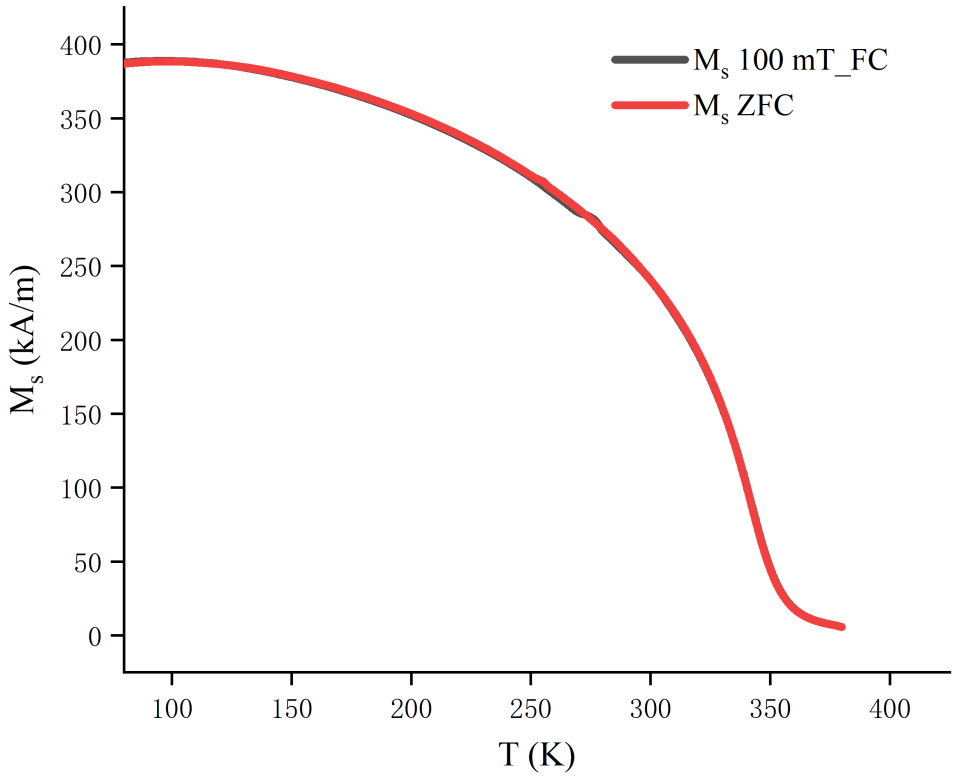

Figure S2. Temperature dependence of saturation magnetization for $Co_8Zn_8Mn_4$ crystal. Temperature-dependent magnetization in zero field-cooled (ZFC) and field-cooled (FC) modes of a magnetic field 100 mT.

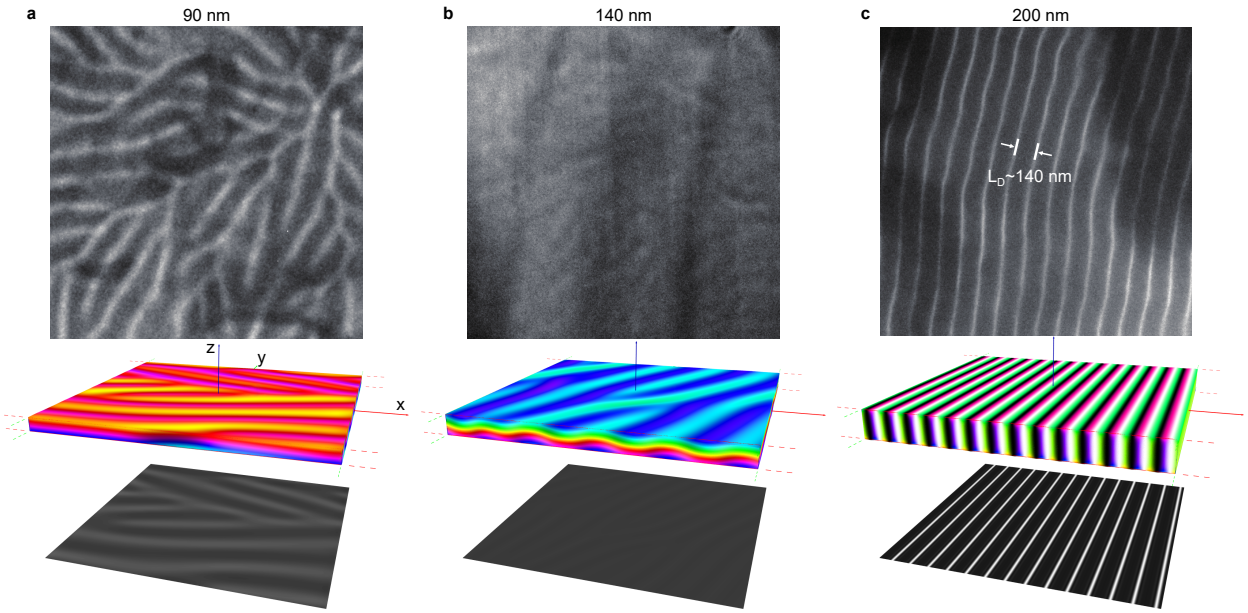

Figure S3. **Spin configurations in $Co_8Zn_8Mn_4$ thin plates of varying thickness.** Ground-state domain structures are shown for samples with thicknesses of 90 nm (**a**), 140 nm (**b**), and 200 nm (**c**). The top row displays experimental Lorentz TEM images for each thickness, with a field of view of $2\,\mu$m $\times$ $2\,\mu$m. In the thickest sample (**c**), a strong Lorentz contrast is observed due to an in-plane helical ground state. The thin samples (**a**, **b**) exhibit helices with out-of-plane wave vectors and additional surface modulations[2]. Compared to in-plane helices, these modulated states yield significantly weaker Lorentz contrast. The amplitude of the surface modulations also oscillates with thickness[3] and becomes especially faint in the 140 nm sample (**b**). The bottom row presents corresponding micromagnetic simulation snapshots and the associated theoretical Lorentz TEM contrasts. The simulated domain in all cases has lateral dimensions of $2\,\mu$m $\times$ $2\,\mu$m and the respective sample thicknesses. The simulations were performed at zero applied magnetic field. The experimental measurements were conducted at a weak magnetic field of about 9 mT.

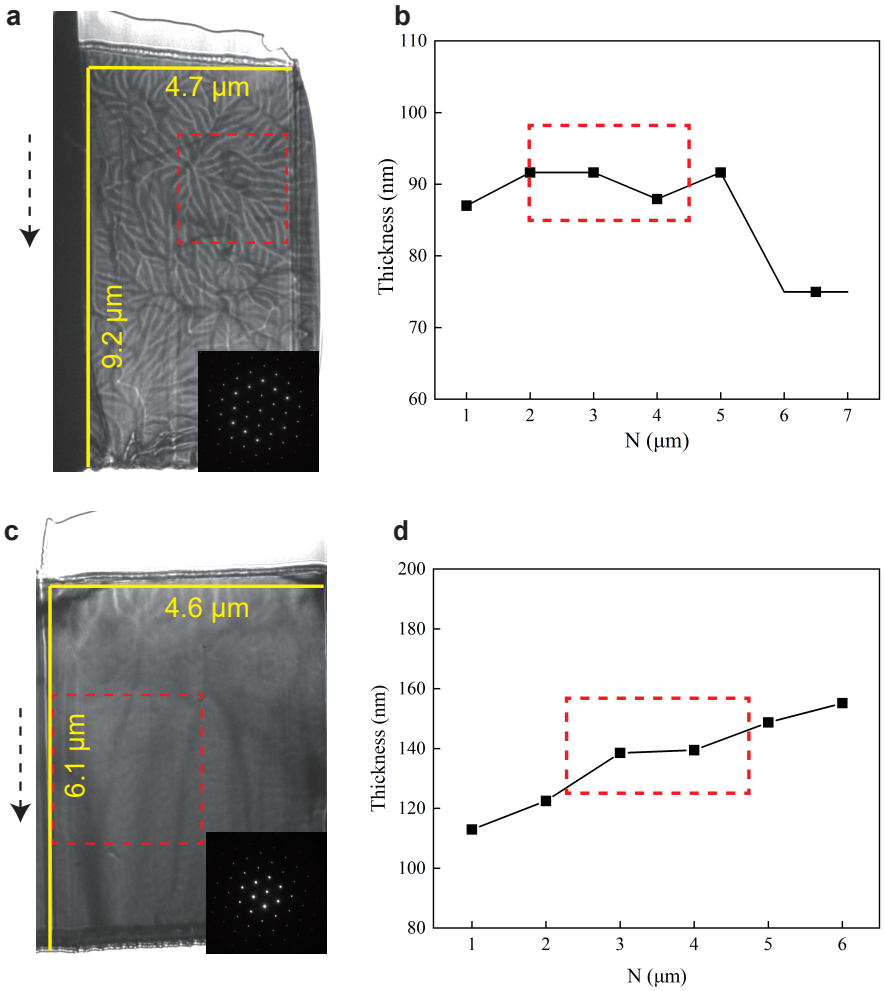

Figure S4. **Characterization of $Co_8Zn_8Mn_4$ thin plate. a** and **c**, Underfocus Lorentz TEM images of $Co_8Zn_8Mn_4$ thin plate under a small magnetic field of $\sim$ 9 mT, with a thickness of $\sim 0.65L_D$ (**a**) and $\sim 1L_D$ (**c**),respectively. Insets show selected-area electron diffraction (SAED) images confirming crystal orientation near the [111] zone axis. Red dash box regions indicate experimental observation areas. **b** and **d**, Corresponding mean thickness profiles along the dashed arrow direction derived from electron energy loss spectroscopy (EELS) point-scan measurements for samples (**a**) and (**c**), respectively.

3. Femtosecond laser-induced bimeron nucleation. Femtoseconds laser excitation induces an instantaneous temperature rise in the electron system within one picosecond. Hot electrons transfer angular momentum to the phonon system through spin-flip scattering, leading to disordering of the spin system and magnetization quenching[4]. At this stage, the magnetic state exhibits loss of long-range magnetic order while retaining partial short-range spin correlation[5], identical to the initial state in Fig. S5**a**. The system evolves toward a relaxed configuration through the minimization of the micromagnetic energy functional, simulating the physical relaxation dynamics that follow laser-induced excitation (Fig. S5). As thermal equilibrium is established between the electron and lattice subsystems, the short-range ordered spins become localized and collectively condense into metastable bimerons.
An ultrafast demagnetized state is achieved following femtosecond laser excitation, quenching the initial magnetization configuration. This state subsequently evolves into a stable final magnetic structure under suitable magnetic field conditions. Crucially, this implies that the excitation outcomes from consecutive laser pulses are mutually independent. Notably, the thermal effects generated by femtosecond laser excitation exhibit prolonged duration, persisting up to microsecond timescales in our samples. When employing high-repetition-rate lasers ($>$ 50 kHz), the inter-pulse interval becomes shorter than the thermal dissipation time. This leads to thermal accumulation that couples the excitation effects between pulses, thereby compromising their independence. Consequently, under identical environmental conditions, consistent results are obtained using low-repetition-rate laser excitation. As demonstrated in Fig. S6, we first saturated the sample magnetization, then applied a 30 mT field to establish identical initial conditions. Subsequent 1-second irradiation using 1 Hz, 10 Hz, and 100 Hz repetition rates all produced identical bimeron configurations.

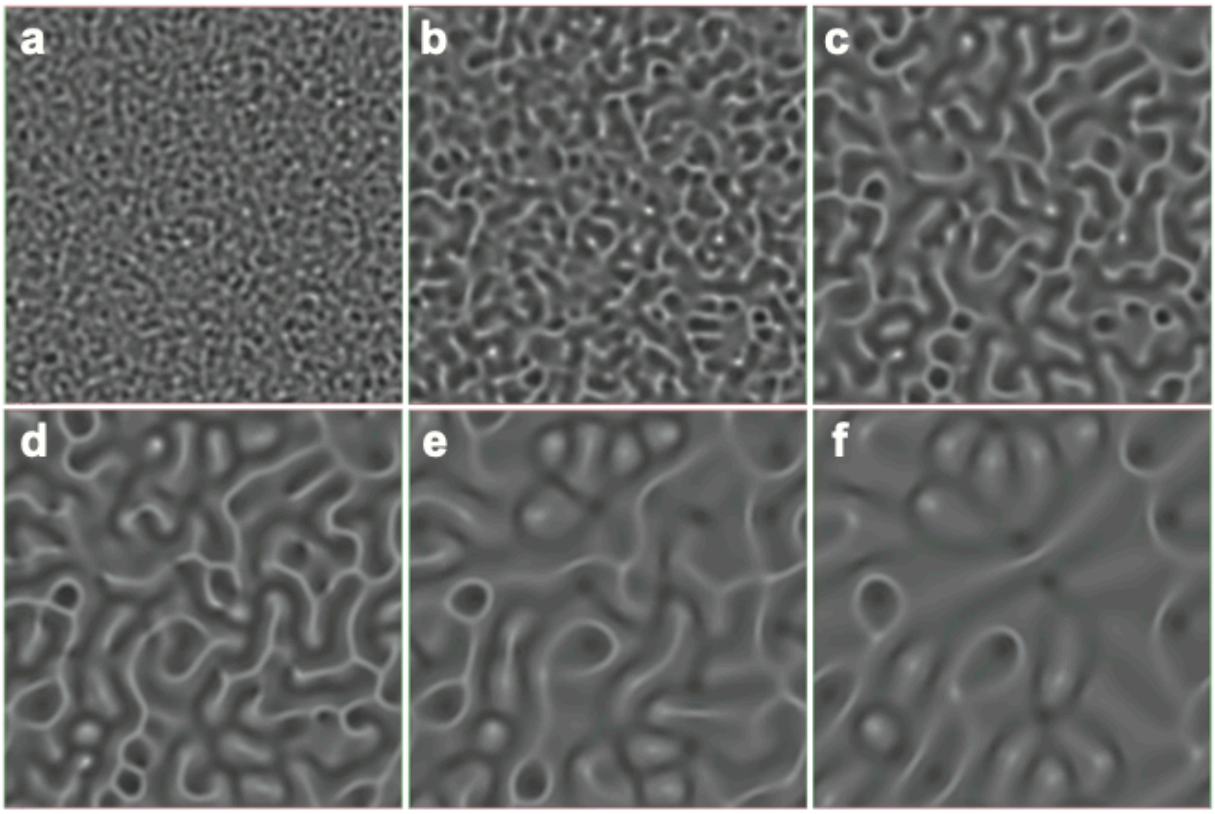

Figure S5. **Simulation of bimerons nucleation in a thin plate of $Co_8Zn_8Mn_4$ under zero magnetic field.** The sequence of images shows the theoretical Lorentz TEM contrast corresponding to spin textures at successive stages of energy minimization, starting from a random initial magnetization. These micromagnetic simulations illustrate the system's evolution toward a relaxed configuration, mimicking the physical relaxation dynamics that follow laser-induced excitation.

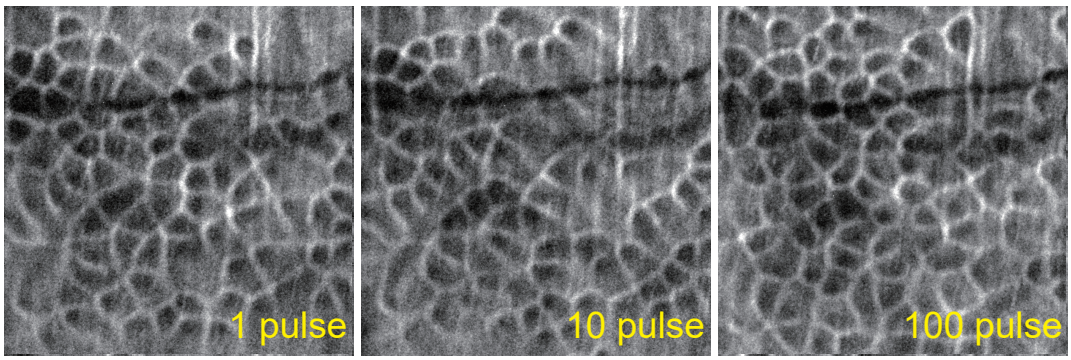

Figure S6. **Final state as a function of number of laser pulses.** At the identical laser fluence of 4.77 mJ/cm^2 and magnetic field of 30 mT, remarkably consistent bimeron structures formed upon laser pulse excitation across repetition frequencies of 1 Hz, 10 Hz, and 100 Hz. The images have identical sizes of around 2.5 μm × 2.5 μm and have been extracted from larger fields of view.

4. Field-cooling manipulation of $Co_8Zn_8Mn_4$ thin plate.

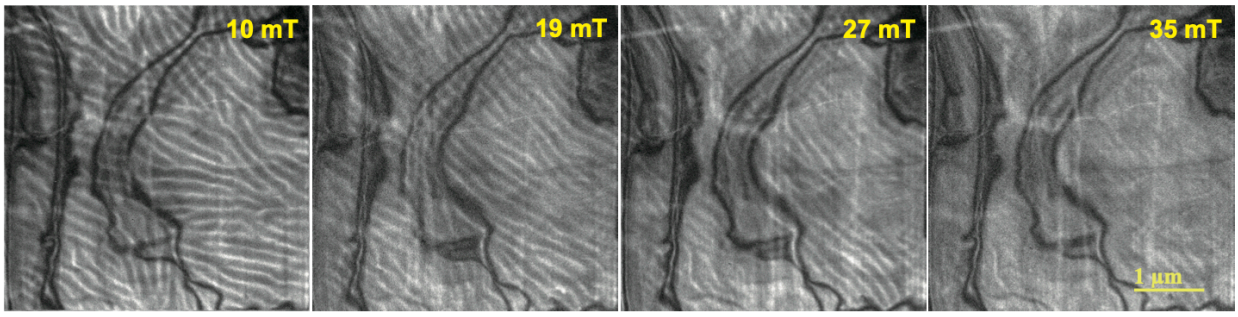

Figure S7. **Field-cooling manipulation under different magnetic fields in $Co_8Zn_8Mn_4$ thin plate.** The domain structures obtained after cooling from 360 K to room temperature under various magnetic fields in a $Co_8Zn_8Mn_4$ plate with thickness $t \approx 90$ nm ($\sim 0.65 L_D$). These images illustrate that no topological spin textures were generated throughout the entire field cooling process.

5. Magnetic textures under varying magnetic fields in thin and thick samples.

Figures S8 and S9 show the evolution of laser-induced magnetic textures under varying magnetic fields in a thin sample of $Co_8Zn_8Mn_4$, $t \sim 0.65 L_D$. Figures S10 and S11 show the same for a thick sample of $Co_8Zn_8Mn_4$, $t \sim 1 L_D$. All topological spin textures were acquired with an identical laser fluence of 4.77 mJ/cm^2. All images have identical sizes of around $2.5 \times 2.5 \mu m^2$ and have been extracted from larger fields of view.

Figures S12–S13 demonstrate the evolution of bimerons under perpendicular magnetic fields

in $t \sim 0.65 L_{\mathrm{D}}$ $Co_8Zn_8Mn_4$ thin plate. All images have identical sizes of around $2.5\,\mu$m $\times$ $2.5\,\mu$m and have been extracted from larger fields of view.

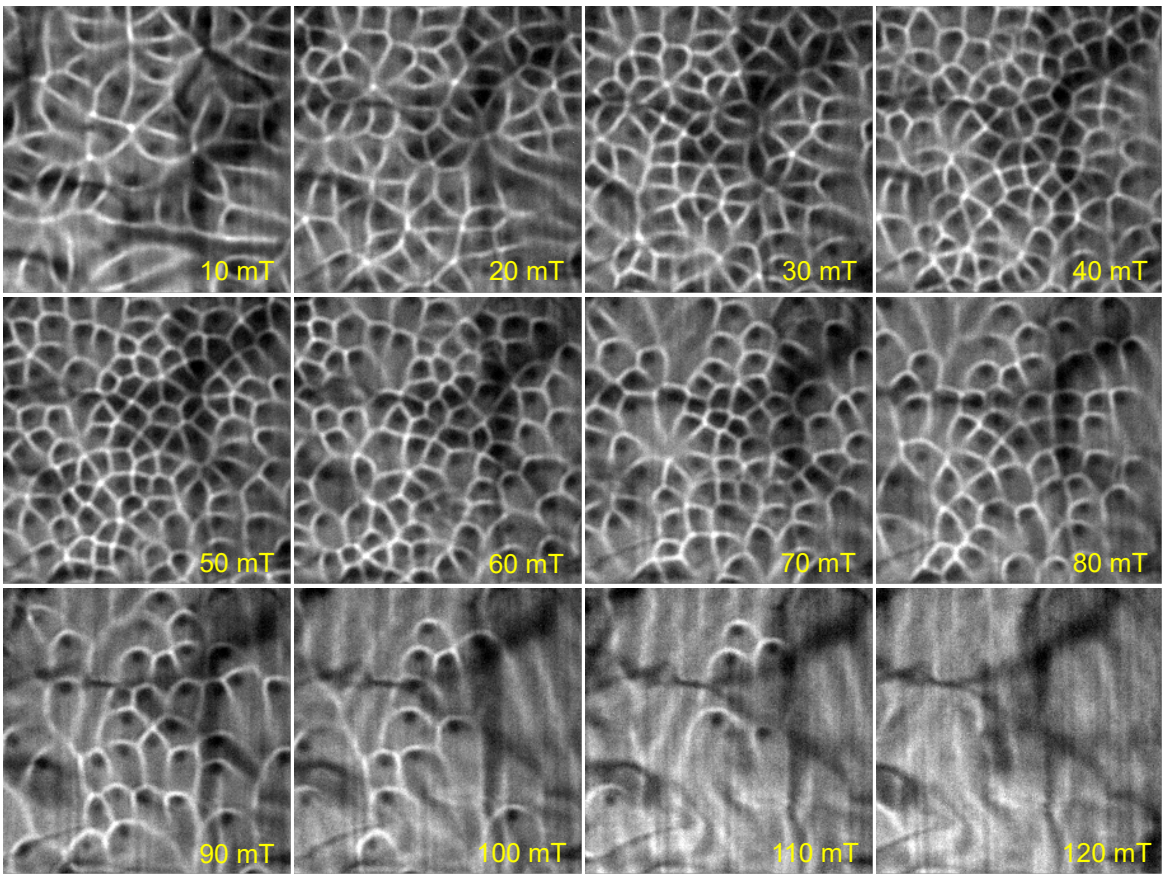

Figure S8. Evolution of laser-induced bimerons in a $Co_8Zn_8Mn_4$ plate under positive out-of-plane magnetic field. The sample has a thickness of approximately $t \approx 90$ nm. The observed bimerons, based on our topological analysis, possess a topological charge of $(1, -1)$, consistent with the configuration shown in Fig. **3b** of the main text. The applied magnetic field is oriented perpendicular to the plane of the sample and directed toward the observer.

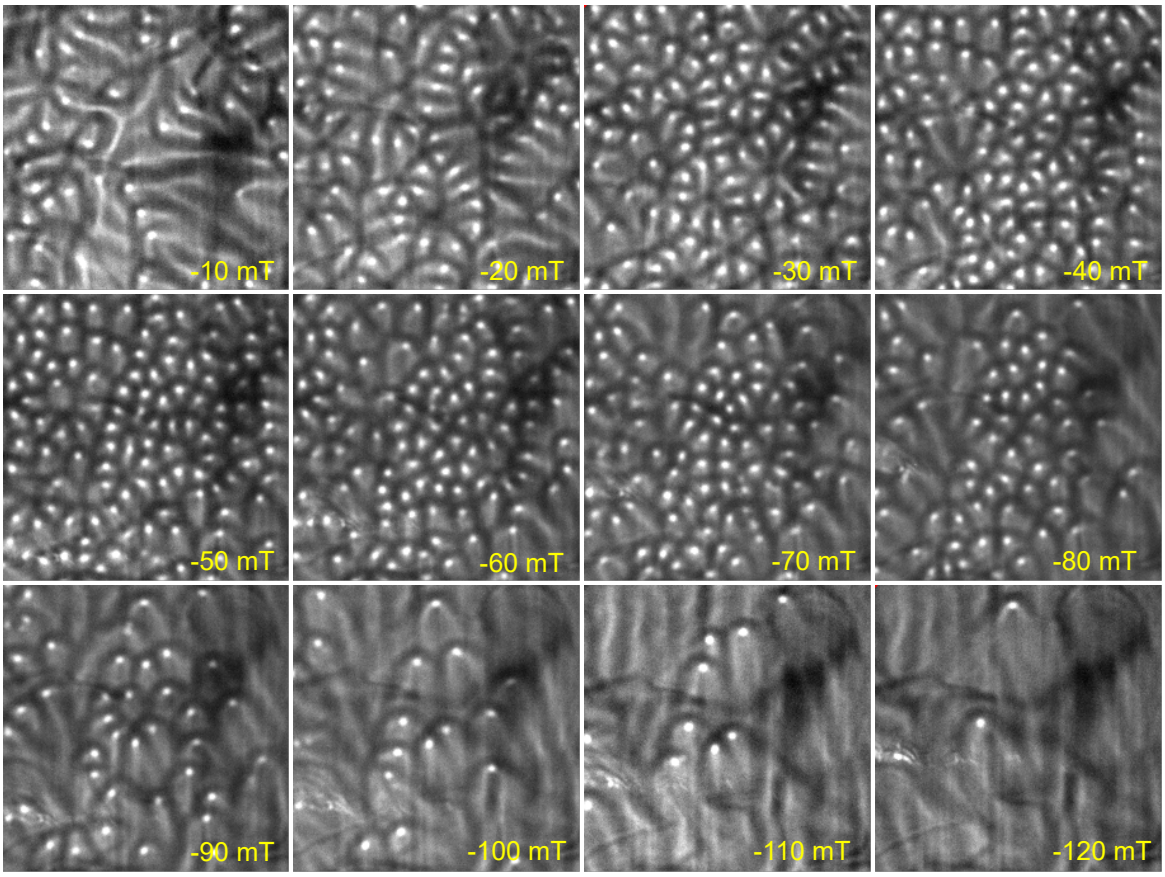

Figure S9. **Evolution of laser-induced bimerons in a $Co_8Zn_8Mn_4$ plate under negative out-of-plane magnetic field.** Same setup as in Fig. S8, but with the applied magnetic field reversed. The out-of-plane magnetic field is now directed away from the observer. The bimerons in this image carry a topological charge of $(-1, 1)$.

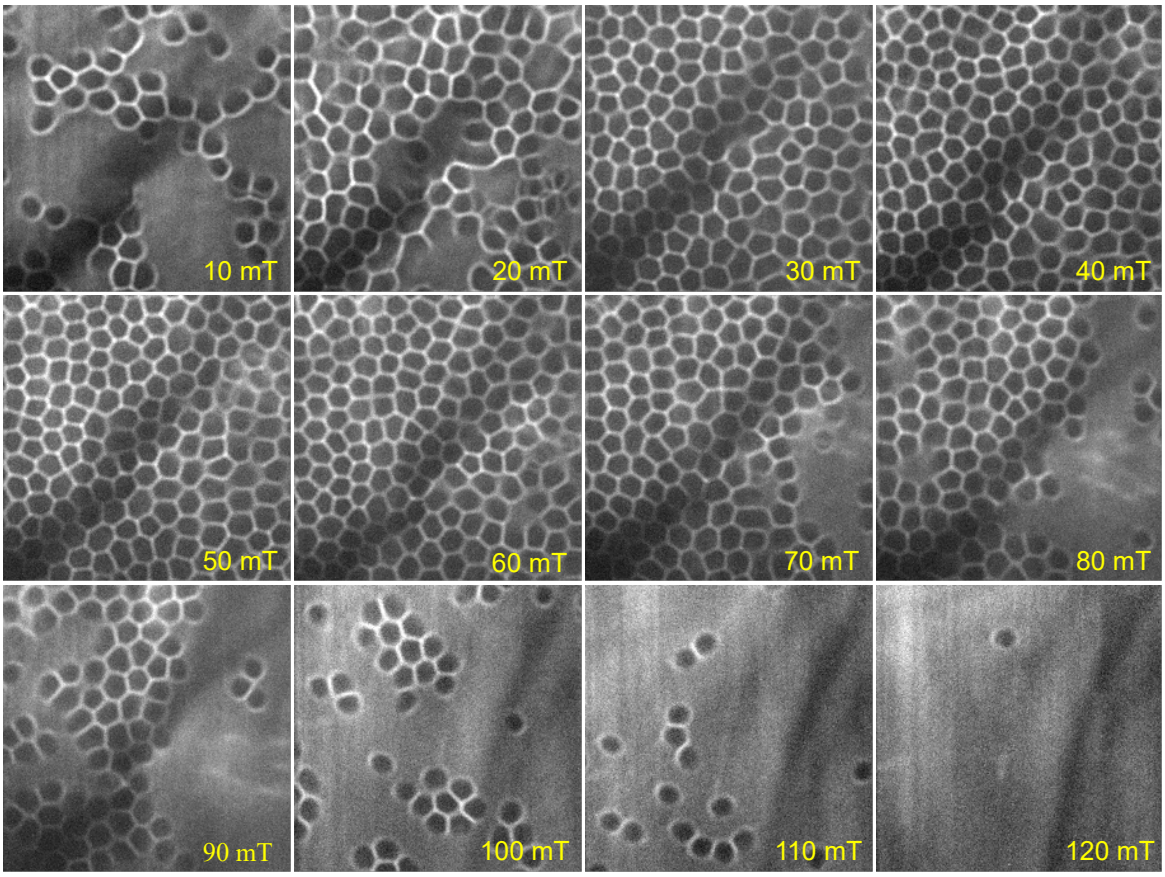

Figure S10. **Evolution of laser-induced bimerons in a $Co_8Zn_8Mn_4$ plate with thickness $t \sim 1L_D$ under positive magnetic fields.** The sample has a thickness of approximately $t \approx 140$ nm. The out-of-plane magnetic field is directed toward the observer. The bimerons in this image carry a topological charge of $(1, -1)$, corresponding to the configuration shown in Fig. **3e** of the main text.

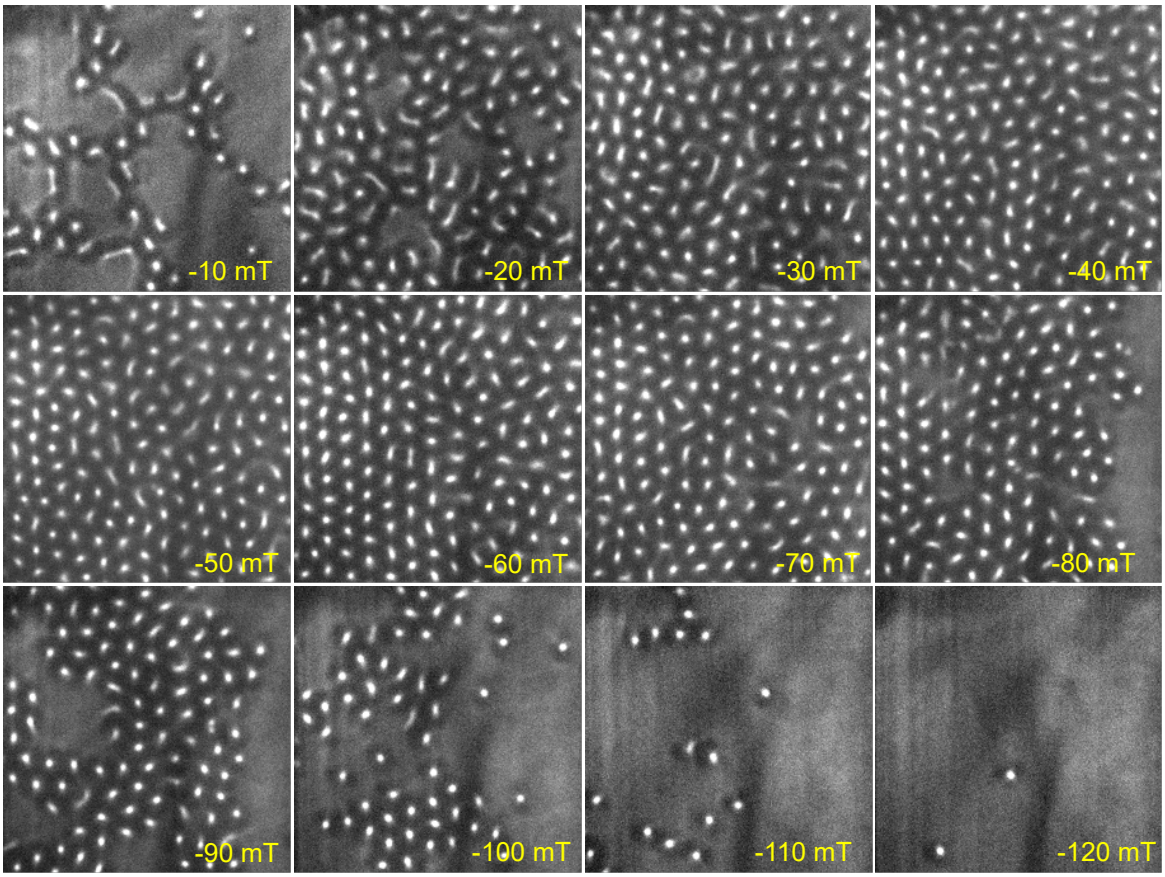

Figure S11. Evolution of laser-induced bimerons in a $Co_8Zn_8Mn_4$ plate with thickness $t \sim 1L_D$ under negative magnetic fields. Same setup as in Fig. S10, but the out-of-plane magnetic field is now directed away from the observer. The bimerons in this image carry a topological charge of $(-1, 1)$.

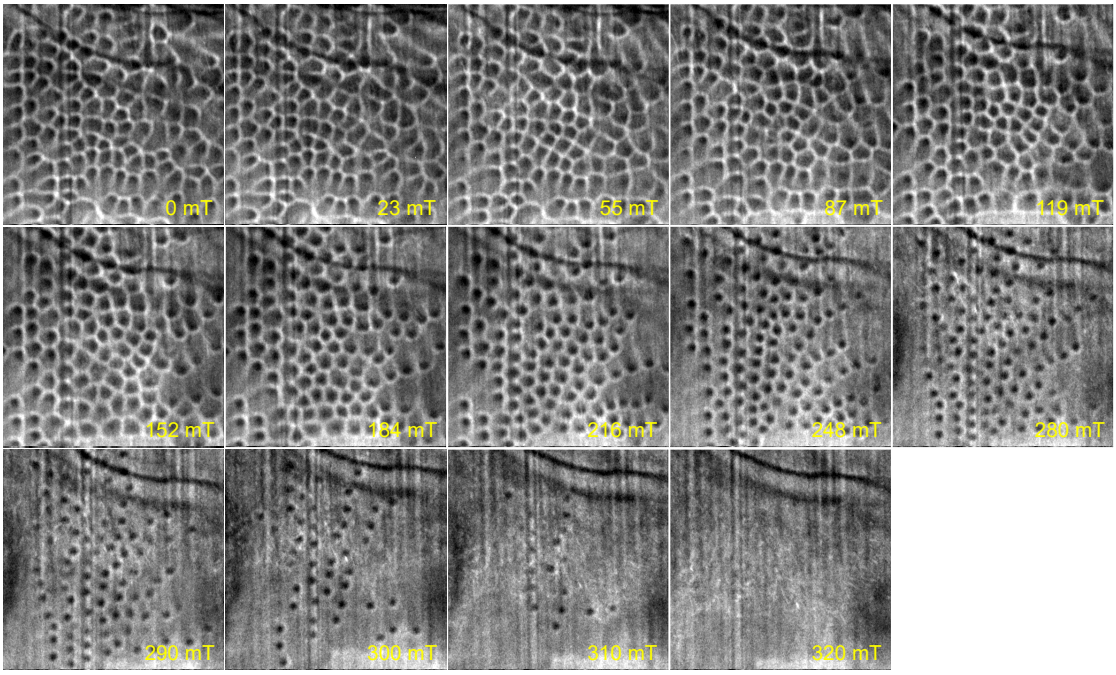

Figure S12. Structural evolution and annihilation of bimerons under increasing perpendicular magnetic fields. Some images from this series are used in Fig. 4 of the main text.

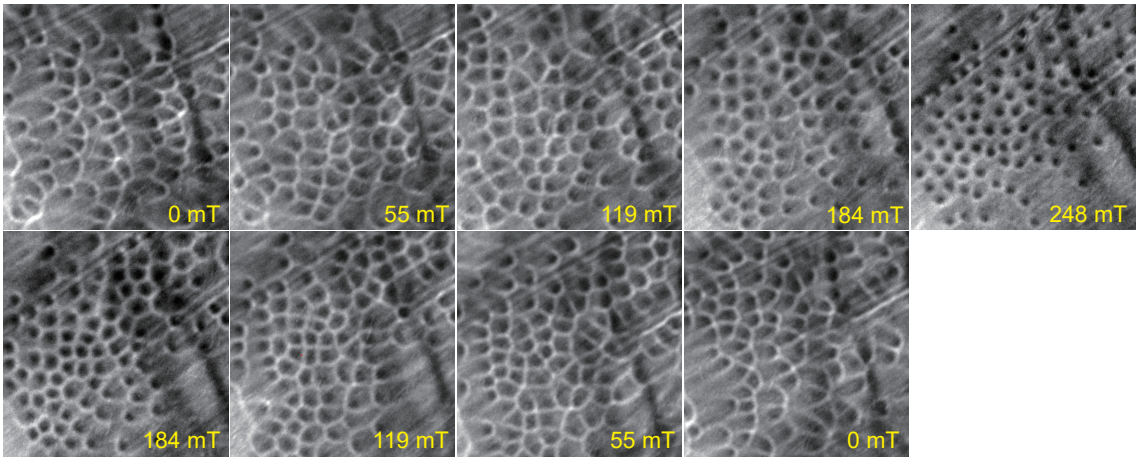

Figure S13. Reversible structural evolution of bimerons under increasing and decreasing perpendicular applied magnetic fields.

[1] Filipp N Rybakov, Olle Eriksson, and Nikolai S Kiselev. Topological invariants of vortices, merons, skyrmions, and their combinations in continuous and discrete systems. *Physical Review B*, 111(13):134417, 2025.

[2] Filipp N Rybakov, Aleksandr B Borisov, Stefan Blügel, and Nikolai S Kiselev. New spiral state and skyrmion lattice in 3d model of chiral magnets. *New Journal of Physics*, 18(4):045002, 2016.

[3] Luyan Yang, Andrii S Savchenko, Fengshan Zheng, Nikolai S Kiselev, Filipp N Rybakov, Xiaodong Han, Stefan Blügel, and Rafal E Dunin-Borkowski. Embedded skyrmion bags in thin films of chiral magnets. *Advanced Materials*, 36(36):2403274, 2024.

[4] B Koopmans, Grégory Malinowski, F Dalla Longa, D Steiauf, M Fähnle, T Roth, M Cinchetti, and M Aeschlimann. Explaining the paradoxical diversity of ultrafast laser-induced demagnetization. *Nature Materials*, 9(3):259–265, 2010.

[5] Ezio Iacocca, T-M Liu, Alexander H Reid, Z Fu, S Ruta, PW Granitzka, E Jal, Stefano Bonetti, AX Gray, CE Graves, et al. Spin-current-mediated rapid magnon localisation and coalescence after ultrafast optical pumping of ferrimagnetic alloys. *Nature Communications*, 10(1):1756, 2019.